PASJ: Publ. Astron. Soc. Japan **47**, 745–760 (1995)

Distribution and Dynamics of Molecular Gas in the Galaxy M51. II. Formation of Giant Molecular Associations and Massive Stars*

Nario KUNO† and Naomasa NAKAI
Nobeyama Radio Observatory,‡ Minamimaki-mura, Minamisaku-gun, Nagano 384-13
E-mail (KN) kuno@nro.nao.ac.jp
and
Toshihiro HANDA and Yoshiaki SOFUE
Institute of Astronomy, The University of Tokyo, Mitaka, Tokyo 181

(Received 1995 April 14; accepted 1995 October 18)

Abstract

We have investigated the distributions of molecular gas, H I-to-H_2 conversion and the formation mechanisms of Giant Molecular Associations (GMAs) and of massive stars in M51 using mapping data of CO obtained with the NRO 45-m telescope. The variations of the molecular-to-total gas mass fraction in the disk and its dependence on the total gas density and the radiation field are shown. The possibilities of a gravitational instability and cloud-cloud collisions as the formation mechanisms of GMAs are examined. A gravitational instability is supported from a comparison between the surface density of the total gas and the critical density of the gravitational instability, as well as from the spatial separations of the GMAs. On the other hand, since the time scale of a cloud-cloud collision is much shorter than the arm-crossing time, cloud coagulation may also work for GMA formation together with a gravitational instability. Point-by-point comparisons between the star-formation rates (SFRs) and the gas surface densities show that the SFR is correlated with the surface density of the total gas better than with that of the molecular gas alone. Observations of ^{13}CO and HCN indicate denser gas in the spiral arms than in the interarms.

Key words: Galaxies: individual (M51) — Galaxies: spiral — Galaxies: structure — ISM: molecules — Stars: formation

1. Introduction

To understand the formation mechanisms of molecular clouds (Giant Molecular Clouds, Giant Molecular Associations) and massive stars in galaxies is one of the most important subjects in astronomy. For molecular-cloud formation, three mechanisms have been proposed: (1) Random collisional agglomeration — small clouds with random motion exchange mass through collisions and form larger clouds (Kwan 1979; Combes, Gerin 1985); (2) The Parker instability — the magnetic Rayleigh-Taylor instability in the interstellar medium is initiated by the passage of a galactic shock, and clouds with masses on the order of $10^5\,M_\odot$ are formed in spiral arms (Parker 1966; Mouschovias et al. 1974); (3) Gravitational instability — the Jeans instability is initiated when the instability condition ($Q < 1$) is satisfied, forming clouds with masses on the order of $10^7\,M_\odot$ (Elmegreen 1990a; Elmegreen et al. 1994). These mechanisms have been reviewed in Elmegreen (1990b). For massive star formation, some mechanisms have also been proposed: (1) self-gravity; (2) cloud-cloud collisions (Scoville et al. 1986); and (3) compression by galactic shock (Woodward 1976). In the case of (1), stars are spontaneously formed by the gravitational collapse of a molecular cloud due to the mass of the cloud, itself, while mechanisms (2) and (3) trigger star formation by inducing a gravitational instability in the compressed regions of the interface between colliding clouds or of the spiral shock. Observational evidence is required to confirm which mechanism actually takes place in the formation of molecular clouds and massive stars in galaxies. Recently, the importance of the large-scale structures of 1–2 kpc has been noticed for star formation in spiral galaxies (Kennicutt 1989): H II regions in galaxies appear in areas in which the total gas density exceeds the critical density of gravitational instability. Actually, many galaxies have star-cloud complexes whose size is comparable to that of superclouds expected to be formed by a gravitational in-

* A part of this work was carried out under the common use observation program at NRO.

† Research Fellow of the Japan Society for the Promotion of Science.

‡ Nobeyama Radio Observatory (NRO) is a branch of the National Astronomical Observatory, an inter-university research institute operated by the Ministry of Education, Science, Sports and Culture.

stability (Elmegreen, Elmegreen 1983). In this paper we examine some mechanisms for the large-scale formation of molecular clouds/associations and of massive stars in the disk of the spiral galaxy M51.

M51 is one of the most suitable galaxies for examining the global distribution of molecular gas and its relation to star formation. It is sufficiently near (9.6 Mpc: Sandage, Tammann 1974) to resolve its spiral arms, has a grand design spiral structure, is almost face on, and shows relatively strong CO emission. M51 has been observed in various frequencies from X-ray to radio; e.g., H I (Rots et al. 1990; Tilanus, Allen 1991), radio continuum (Mathewson et al. 1972; Segalovitz 1977; Klein et al. 1984; van der Hulst et al. 1988), and Hα (Tully 1974a, 1974b, 1974c). These data make it possible to study the formation of molecular clouds and massive stars by making comparisons with CO data. Therefore, many people have made CO observations of this galaxy. Rydbeck et al. (1985) partially mapped CO in the galactic disk and reported an excess of CO intensity in the arms by only 20% compared with that in the interarms under an angular resolution of HPBW = 33″. However, with low resolution (HPBW = 45″), Lord and Young (1989) found from a comparison between the azimuthal variations of CO and Hα that the star-formation efficiency is enhanced in the arms. García-Burillo et al. (1993a) mapped in the $J = 1$–0 and $J = 2$–1 transitions of ^{12}CO with the IRAM 30-m telescope, and García-Burillo et al. (1993b) compared the distributions and kinematics of the molecular gas with numerical simulations. Vogel et al. (1988) showed clear molecular arms using the OVRO interferometer, and resolved them into giant molecular associations (GMAs), whose mass is on the order of $10^7\ M_\odot$. Rand and Kulkarni (1990) mapped almost the entire disk of M51 using the same interferometer, and Rand (1993) studied the properties and formation mechanisms of GMAs in both the arms and interarms.

We have made a full mapping of the CO in M51 using the Nobeyama 45-m telescope. An angular resolution of 16″ (745 pc) is sufficiently high to study the molecular spiral structure in the galaxy. Details concerning the observations and the data were presented by Nakai et al. (1994) (Paper I). In this paper, we show the large-scale distribution of molecular gas (section 2), and discuss the H I-to-H_2 conversion (section 3), formation mechanisms of GMAs (section 4), and massive stars (section 5) in M51. The physical state of the molecular gas is also examined using the results of additional observations of ^{13}CO and HCN (section 6). We will present the kinematics of the molecular gas in a forthcoming paper. The parameters of M51 adopted in this paper are summarized in table 1, and the parameters of the observations are listed in table 2.

Table 1. Parameters of M51.

Center position (1950.0)*	R.A. = $13^h27^m46^s.327$ Decl. = $47°27'10''.25$
Morphological type†‡	Sbc
Systemic velocity (LSR)§	469 ± 5 km s^{-1}
Distance#	9.6 Mpc
Position angle of major axis¶	$-10° \pm 3°$
Inclination angle¶	$20° \pm 5°$ (90° is edge-on)
Beam size on galaxy (16″)	745 pc

* Position of 1.4 GHz radio continuum peak (Ford et al. 1985).
† de Vaucouleurs et al. 1991.
‡ Sandage and Tammann 1981.
§ Details in a forthcoming paper. Corresponding heliocentric velocity is 461 km s^{-1}.
# Sandage and Tammann 1974.
¶ Tully 1974b.

Table 2. Parameters of observations.

	^{12}CO	^{13}CO	HCN
Rest frequency (GHz)	115.271204	110.201353	88.6318473
HPBW (″)	16	17	20
η_a	0.36	0.37	0.39
η_{mb}	0.50	0.52	0.55

2. Distributions of Molecular Gas

2.1. *CO-to-H_2 Conversion Factor*

The H_2 column density $N(H_2)$ cm^{-2} in external galaxies is usually derived from the CO integrated intensity (I_{CO} K km s^{-1}) using the empirically determined CO-to-H_2 conversion factor. The conversion factor has been estimated to be $\alpha = N(H_2)/I_{CO} = (1\text{–}5) \times 10^{20}$ cm^{-2} (K km s^{-1})$^{-1}$ in our Galaxy (e.g., Scoville, Sanders 1987; Solomon et al. 1987, and references therein) and $(0.5\text{–}60)\times10^{20}$ cm^{-2} (K km s^{-1})$^{-1}$ in external galaxies (Nakai, Kuno 1995 and references therein). In M51, the factor has been evaluated to be 1.2×10^{20} cm^{-2} (K km s^{-1})$^{-1}$ based on the virial-mass method (Adler et al. 1992), 1.8 and 0.8×10^{20} cm^{-2} (K km s^{-1})$^{-1}$ from visual extinction and Monte-Carlo radiative-transfer calculations (García-Burillo et al. 1993a), and 0.9×10^{20} cm^{-2} (K km s^{-1})$^{-1}$ from visual extinction (Nakai, Kuno 1995). Here, we use the following conversion factor for M51:

$$N(H_2) = 1.0 \times 10^{20} I_{CO} \ \text{cm}^{-2}, \quad (1)$$

where $I_{CO} \equiv \int T_{mb} dv$ K km s^{-1} and $T_{mb} \equiv T_A^*/\eta_{mb}$ K (η_{mb} is the main beam efficiency). This is equivalent to

Table 3. Masses in M51.

	$R < 1$ kpc	$R < 8$ kpc
M (H I) ($M_\odot$)	1.6×10^7	2.5×10^9
M (H_2) ($M_\odot$)	5.6×10^8	5.5×10^9
M (H II)* ($M_\odot$)	6.9×10^6	6.4×10^8
$M_{\rm dyn}$† ($M_\odot$)	7.0×10^9	8.0×10^{10}

* The electron temperature of 10^4 K and the scale height of 200 pc are assumed.
† A spherical mass distribution is assumed.

$$\sigma(H_2) = 1.59\ I_{\rm CO}\ \ M_\odot\ {\rm pc}^{-2}. \quad (2)$$

This gives a 2- or 3-times smaller value than the conversion factor generally used in our Galaxy [e.g., 2.6×10^{20} cm^{-2} (K km s^{-1})$^{-1}$; Bloemen et al. 1984]. Although the dependence of the conversion factor on the CO intensity has been pointed out by Nakai and Kuno (1995), further studies are required to accurately determine the dependence. Thus, we use the constant factor for any $I_{\rm CO}$.

2.2. *Radial Distributions*

Figure 1 shows the radial distributions of the surface mass density of the molecular gas $\sigma(H_2)$, atomic gas σ(H I), total neutral gas σ(H I+H_2), and Hα flux density in M51, where we used H I data of Rots et al. (1990) and Hα data of Tully (1974a). The molecular gas is distributed mainly in the inner disk of M51, and its surface density decreases outward with an exponential shape of $245 \exp[-R\ {\rm kpc}/2.0]\ M_\odot\ {\rm pc}^{-2}$ at a radius (R) of 1.5–5 kpc. At $R < 1.5$ kpc, the molecular gas is depleted, compared with the exponential fitting curve (also see figure 2a). At $R \approx 6$ kpc, $\sigma(H_2)$, also, the Hα flux is enhanced. This may be caused by an interaction with the companion galaxy NGC 5195 (the disk of M51 is affected by this interaction only at $R \geq 6$ kpc; Paper I). It is apparent that the molecular gas is dominant in the inner disk and that $\sigma(H_2)/\sigma$(H I) ≈ 1 at about 8 kpc (see also figure 6). The molecular gas mass ($5.5 \times 10^9\ M_\odot$) represents about 64% of the total gas mass ($8.6 \times 10^9\ M_\odot$) and 7% of the dynamical mass ($8 \times 10^{10}\ M_\odot$) within $R \approx 8$ kpc, where the dynamical mass within the galactocentric radius (R kpc) is calculated from

$$M_{\rm dyn} = 2.25 \times 10^5\ RV^2\ M_\odot, \quad (3)$$

assuming a spherical distribution of the mass (V km s^{-1} is the rotational velocity at R). In the central region ($R <$ 1 kpc), the molecular gas mass ($5.6 \times 10^8\ M_\odot$) represents about 96% of the total gas mass ($5.8 \times 10^8\ M_\odot$) and 8% of the dynamical mass ($7 \times 10^9\ M_\odot$).

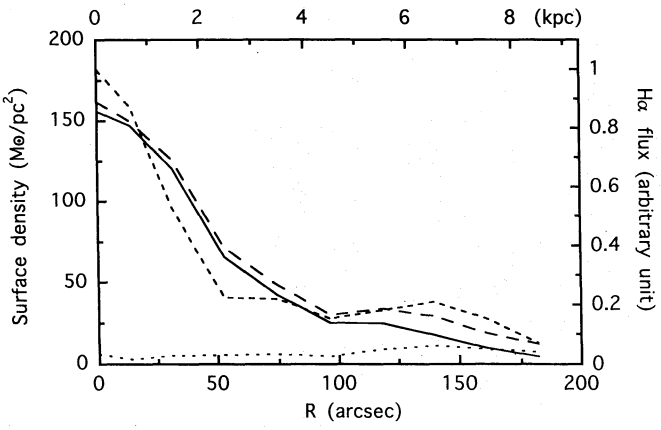

Fig. 1. Radial distributions of the H_2 surface density, $\sigma(H_2)\ M_\odot\ {\rm pc}^{-2}$, (solid line), H I surface density, σ(H I) $M_\odot\ {\rm pc}^{-2}$, (dotted line), total gas surface density, σ(H I+H_2) = $\sigma(H_2) + \sigma$(H I) $M_\odot\ {\rm pc}^{-2}$, (long dashed line), and Hα flux density (dashed line) in M51.

2.3. *Molecular Spiral Structure*

Figure 2a shows a map of the CO integrated intensity ($I_{\rm CO}$) presented in Paper I. We can easily trace two molecular spiral arms, which are nearly logarithmic spirals with a pitch angle of about 20° at $40'' < R < 120''$ (2 kpc $< R <$ 5.5 kpc). The maps of H I and Hα are also shown in figures 2b and 2c for a comparison. The maps of CO and Hα are generally correlated with each other. [The CO clumpy structures seem to have about the same size 1–2 kpc as that of the clumps in Hα map.] In more detail, however, we find some differences between them. As mentioned in Paper I, the Hα arms are shifted downstream from the CO arms by about 440 pc. The intensity of the Hα arms is almost constant with radius, while the CO arms become weaker in the outer regions. On the other hand, the H I arms become stronger in the outer regions and the arm structure of H I is not clear in the inner region, because most neutral gas is in the form of molecules there. Figure 3 shows the variations of $I_{\rm CO}$ along two arms. As mentioned in Paper I, the arms are clumpy. These clumps (peaks of $I_{\rm CO}$) correspond to continuum peaks in Segalovitz (1977) and GMAs in Rand and Kulkarni (1990) and Tosaki et al. (1994). The spacing between the clumps increases with the distance from the center (see section 4).

Figure 4 shows the azimuthal variations of $I_{\rm CO}$, where the azimuthal angle is measured from the eastern side of the minor axis (P.A. = 80°) counterclockwise. Figure 5 shows the arm-to-interarm ratio of $I_{\rm CO}$ as a function of the galactocentric radius. The arm-to-interarm ratio is 1.5–7 in this range, having a minimum value at $R =$ $80''$–$100''$, where the arms are discontinuous (figure 2a),

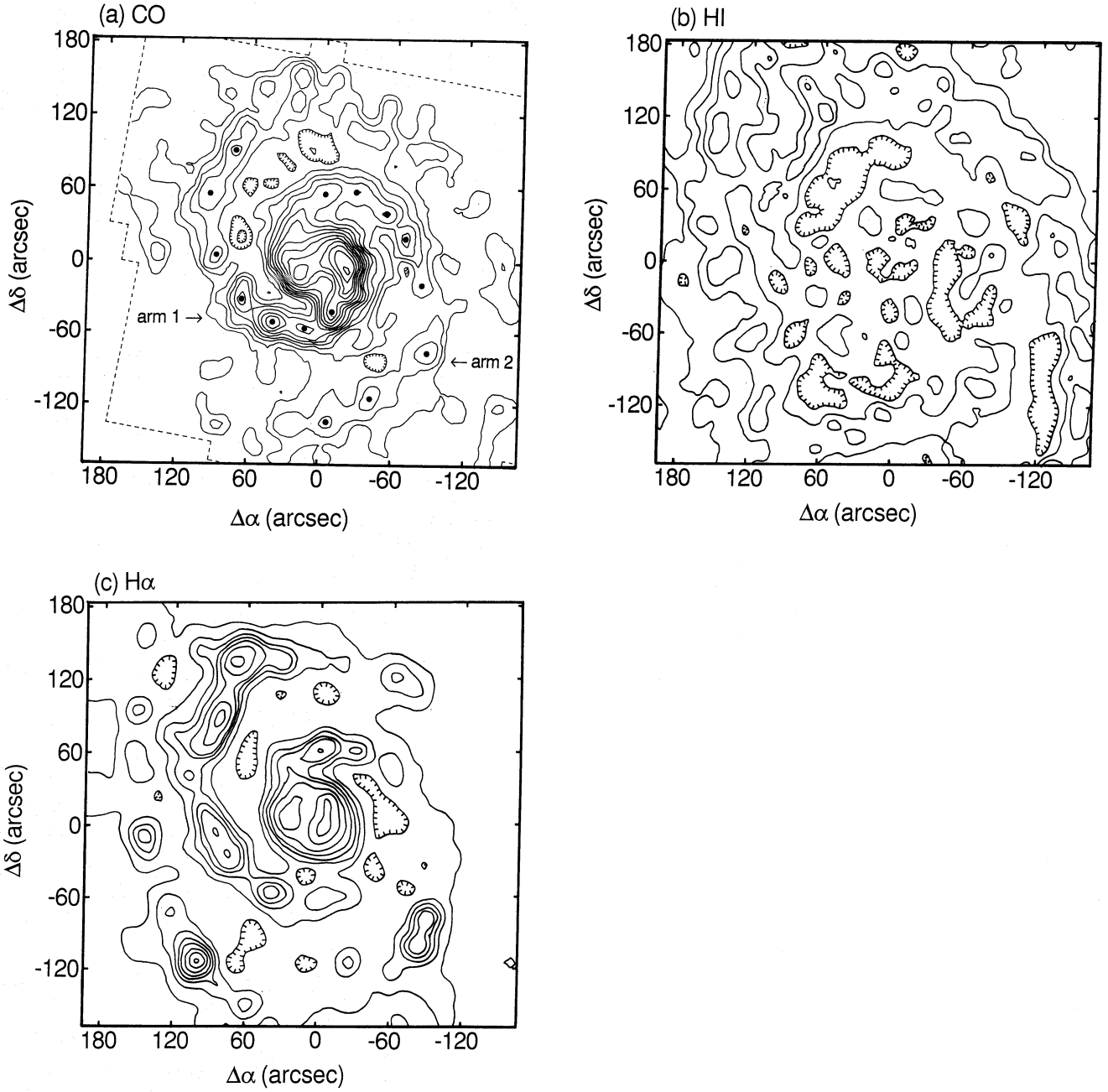

Fig. 2. (a) Contour map of the CO integrated intensity (Nakai et al. 1994), $I_{CO} \equiv \int T_{mb} dv$ K km s^{-1}. The observing area is represented by the dotted line. The first contour and contour interval are 8 K km s^{-1}. The filled circles indicate the positions of the I_{CO} peaks as GMA positions. (b) Contour map of the H I flux density (Rots et al. 1990). Contour values are 100, 300, 500, 700 mJy km s^{-1}beam^{-1}. The map is smoothed to the same spatial resolution (16″) as (a). (c) Contour map of the Hα flux density (Tully 1974a). Contour values are 1.3, 2.6, 3.9, 5.2, 6.5, 9.1, 11.7, 14.3 erg s^{-1}cm^{-2}arcsec^{-2}. The map is smoothed to the same spatial resolution (16″) as (a).

and increasing with the radius beyond $R \approx 100''$. The radial variations of the arm-to-interarm ratio are quite consistent with the results obtained with the IRAM 30-m telescope (García-Burillo et al. 1993a). From figures 2a and 5, it is apparent that I_{CO} is systematically stronger in arm 1 than in arm 2. The same property can be seen in Hα (Tully 1994a).

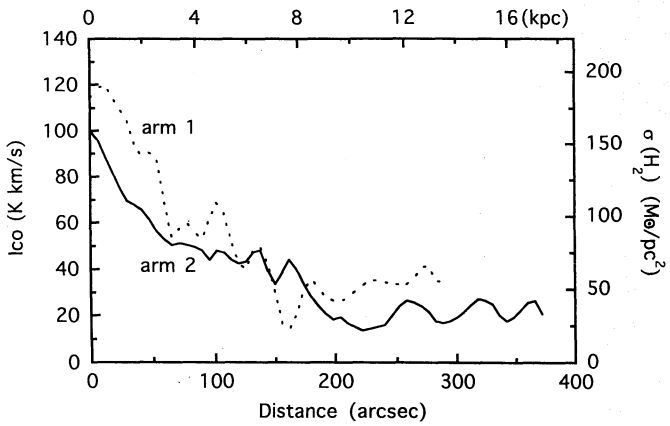

Fig. 3. CO integrated intensity along the spiral arms. The dotted line and the solid line represent arm 1 and arm 2, respectively (figure 2a). The distance is measured along each arm from $R = 20''$, P.A. = $-65°$ for arm 1 and $R = 20''$, P.A. = $115°$ for arm 2. Note that the peaks of the CO intensity of arms 1 and 2 are located at almost same positions as each other at $< 150''$, while peaks of arm 1 seem to be roughly at the positions of the minimum intensity of arm 2 at $> 150''$.

3. H I-to-H_2 Conversion

Here, we examine the formation of molecular gas in M51 by comparing it with high-resolution H I data (figure 2b). Figure 6 shows the radial variation of the molecular mass fraction, $f_{\rm mol} = \sigma({\rm H_2})/\sigma({\rm H\,I+H_2})$ (filled circles). The fraction of molecular gas decreases with the radius, and becomes 50% at about 8 kpc. Figure 7 shows the azimuthal variations of $f_{\rm mol}$. In the inner region ($R \leq 70''$), $f_{\rm mol}$ is almost constant in the arms and the interarms. On the other hand, $f_{\rm mol}$ in the interarms decreases in the outer region at $R \geq 100''$. In M51, it is suggested that H I in the arms is a product of photodissociation of H_2 by newly born massive stars (Tilanus, Allen 1989). Actually, at some radius (e.g., $R = 80''$–$90''$), $f_{\rm mol}$ decreases in the arms. The enhancement of $f_{\rm mol}$ in the interarm regions is about 10%, which is consistent with the estimation of Tilanus and Allen (1989). Figure 8a shows the dependence of $f_{\rm mol}$ on the total gas surface density. We plotted the dependence separately for regions with $F({\rm H}\alpha) > 3.3 \times 10^{-16}$ erg s^{-1}cm^{-2}arcsec^{-2} (triangles) and $F({\rm H}\alpha) < 3.3 \times 10^{-16}$ erg s^{-1}cm^{-2}arcsec^{-2} (circles) in order to see the dependence of $f_{\rm mol}$ on the intensity of radiation field. From the figure, it is clear that $f_{\rm mol}$ decreases with the strength of the radiation field and increases with the total gas surface density. Therefore, $f_{\rm mol}$ in the arms, where radiation is much stronger than in the interarms, becomes smaller than that in the interarms, if the arm-to-interarm ratio of the surface density of the total gas is small, like at $R = 80''$–$90''$.

Elmegreen (1993b) has analyzed $f_{\rm mol}$ quantitatively using the shielding function derived from Federman et al. (1979). In his calculations, he assumed that interstellar clouds consist of diffuse clouds and self-gravitating dense clouds, regardless of the molecular or atomic phase. The molecular-mass fraction in each cloud is determined by the shielding function, depending on the gas density of the clouds, the intensity of the radiation field, and the metallicity. The fraction of the self-gravitating cloud and the gas density of each cloud depend on the external pressure. As a result, he showed that $f_{\rm mol}$ strongly depends on the external pressure or the surface density of the total gas (because the external pressure is assumed to be proportional to the square of the surface density of the total gas). We applied the Elmegreen (1993b)'s model to M51 in order to compare it with our observational results. In his model, all of the parameters (external pressure, metallicity, and intensity of radiation field) are scaled with the values in the solar neighborhood. We used the surface density of the total gas, oxygen abundance and Hα flux to determine the external pressure, the metallicity and the intensity of the radiation field, respectively. As the values in the solar neighborhood we adopted a surface gas density of $8\,M_\odot$ pc^{-2} (Sanders et al. 1984), an oxygen abundance of 0.00065 [$12 + \log({\rm O/H}) = 8.81$: Shaver et al. 1983] and an Hα flux of 2.42×10^{-7} erg cm^{-2}s^{-1}sr^{-1} (Reynolds 1984). The oxygen abundance and Hα flux in M51 are referred from Zaritsky et al. (1994) and Tully (1974a), respectively. The results of the calculations are shown in figure 6 (open circles) and figure 8b. The model agrees with the observational radial distribution of $f_{\rm mol}$, and also agrees with the dependence of $f_{\rm mol}$ on the surface density of the total gas and the intensity of the radiation field shown in figure 8a, although the dependence of the calculated $f_{\rm mol}$ on the total gas surface density seems to be stronger than the observational results. These results suggest that the central depletion of H I seen in most spiral galaxies may be due to the high self-shielding ability, because of the high pressure in the central regions.

4. Formation of Giant Molecular Associations

Figure 2a shows some clumpy structures (filled circles) in the arms which correspond to Giant Molecular Associations (GMAs) found by Vogel et al. (1988). The mass of GMAs is 10^7–$10^8\,M_\odot$. The mechanism of GMA formation has been studied mainly based on observations with interferometers (Rand 1993; Tosaki et al. 1994). In this section we discuss the possibility of GMA formation due to a gravitational instability and random collisional agglomeration based on the present data.

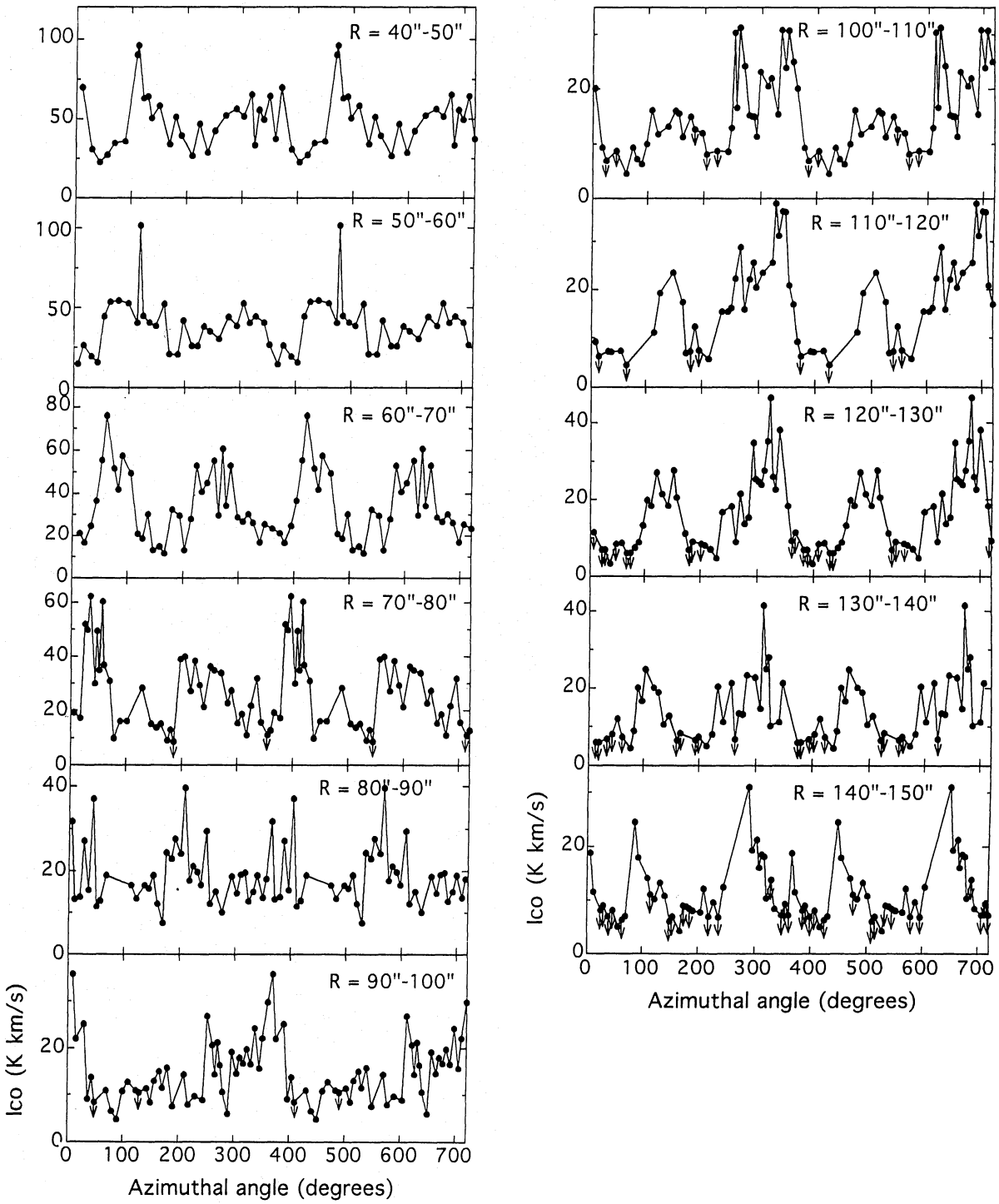

Fig. 4. Azimuthal variations of the CO integrated intensity, corrected for the inclination of the galaxy. The azimuthal angle is measured from the eastern side of the minor axis (P.A. = 80°) counterclockwise. The galactocentric radius is shown at the top right in the boxes.

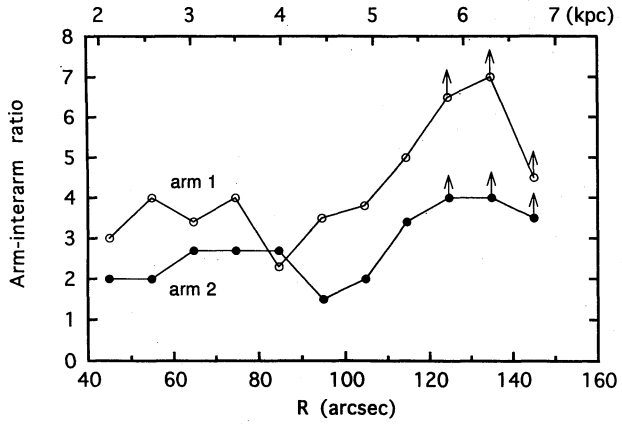

Fig. 5. Arm-to-interarm ratios of the CO integrated intensity as a function of galactocentric radius. Arm 1 and arm 2 are represented by open circles and filled circles, respectively.

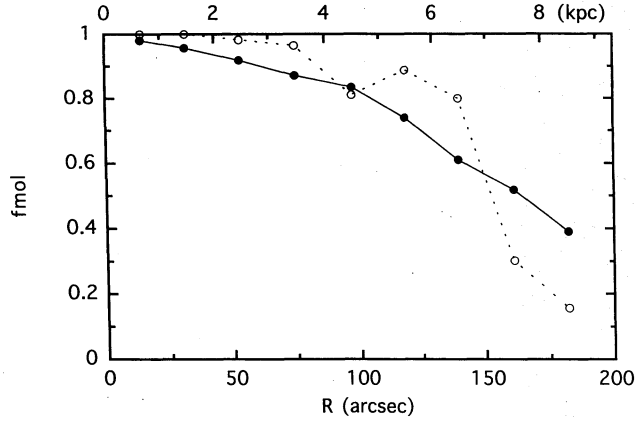

Fig. 6. Molecular mass fraction, $f_{\rm mol} = \sigma({\rm H_2})/\sigma({\rm H\,I} + {\rm H_2})$, as a function of the galactocentric radius. The filled circles and the open circles represent the observed and calculated results (see text), respectively.

4.1. *Gravitational Instability*

The most probable mechanism of GMA formation is a gravitational instability. In a thin isothermal gas disk, large-scale density perturbations are expected to grow when the surface density of total gas exceeds a critical density of the instability, due to the self-gravity of the gas,

$$\sigma_{\rm c} = \frac{\alpha \kappa c}{\pi G}, \qquad (4)$$

where κ is the epicyclic frequency, G the gravitational constant, α a dimensionless constant (Toomre 1964), and $c = (\gamma_{\rm eff} c_{\rm t}^2 + v_{\rm A}^2)^{1/2}$ is the effective velocity dispersion [c should not be too much different from $c_{\rm t}$ (Elmegreen et al. 1994)], where $\gamma_{\rm eff}$ is the effective ratio of the specific heats (Elmegreen 1991), $c_{\rm t}$ the turbulent speed, $v_{\rm A}$ the Alfvén speed. Kennicutt (1989) gave $\alpha = 0.5$–0.85 in disk galaxies. We checked the criterion for a gravitational instability through the disk of M51 by comparing the surface density of the total gas $\sigma({\rm H\,I}+{\rm H_2})$, including heavy elements, with the critical density. We adopted $\alpha = 0.67$, which best fits the observed star-formation thresholds in Kennicutt (1989), the constant rotation velocity of 200 km s^{-1} and the observed velocity dispersion, which gradually decreases with the radius from 17 km s^{-1} at $R = 30''$ to 11 km s^{-1} at $R = 150''$. Figure 9 shows the map of $\sigma({\rm H\,I}+{\rm H_2})/\sigma_{\rm c}$. The gray scale shows the region where the criterion is satisfied, i.e., $\sigma({\rm H\,I}+{\rm H_2})/\sigma_{\rm c} > 1$, while the region where the criterion is not satisfied is white. There are no data for the central region of $R < 30''$, because it is difficult to derive the velocity dispersion due to the large velocity gradient in the beam. Obviously, the criterion is satisfied in most of the arms, while there are few places where the ratio exceeds unity in the interarms.

Under a gravitational instability, the separation between GMAs is expected to be the wavelength of the fastest growing mode, which depends on the gas density: Elmegreen (1994) expressed the wavelength as

$$\lambda = 2.2 \left(\frac{c}{7 \text{ km s}^{-1}} \right)^2 \left(\frac{\sigma}{20\, M_\odot \text{ pc}^{-2}} \right)^{-1} \text{kpc}, \qquad (5)$$

where σ is the mass column density of the gas. Figure 10 shows the observed λ as a function of $\sigma({\rm H_2})$ averaged between the CO peaks in figure 3. We used the surface density of only molecular gas, including He and heavy elements. If we use the surface density of the total gas, including atomic gas, the surface density at a given λ shifts to a higher value by only 10–20%. The observed λ can be fitted with equation (5) assuming a constant velocity dispersion, as shown by the curve in figure 10. The velocity dispersion derived from the fitting is 12 km s^{-1}, which is consistent with the observed velocity dispersion (17 km s^{-1} at $R = 30''$ to 11 km s^{-1} at $150''$). Since the surface density σ decreases with the radius (figure 3), the observed radial gradient of the velocity dispersion causes a slower decrease of the observed λ than the fitted curve in figure 10, and a larger separation in the central region. The good agreement between the calculated and observed separations of GMAs supports the gravitational instability as a formation mechanism of GMAs. It may also indicate that the spiral arms are young and in an early stage of evolution, as suggested by numerical simulations (Howard, Byrd 1990), and that the GMAs were formed as the first gas collapse (Elmegreen 1993a). However, we must note that the results of the above analyses are altered if the Galactic conversion factor is used: since

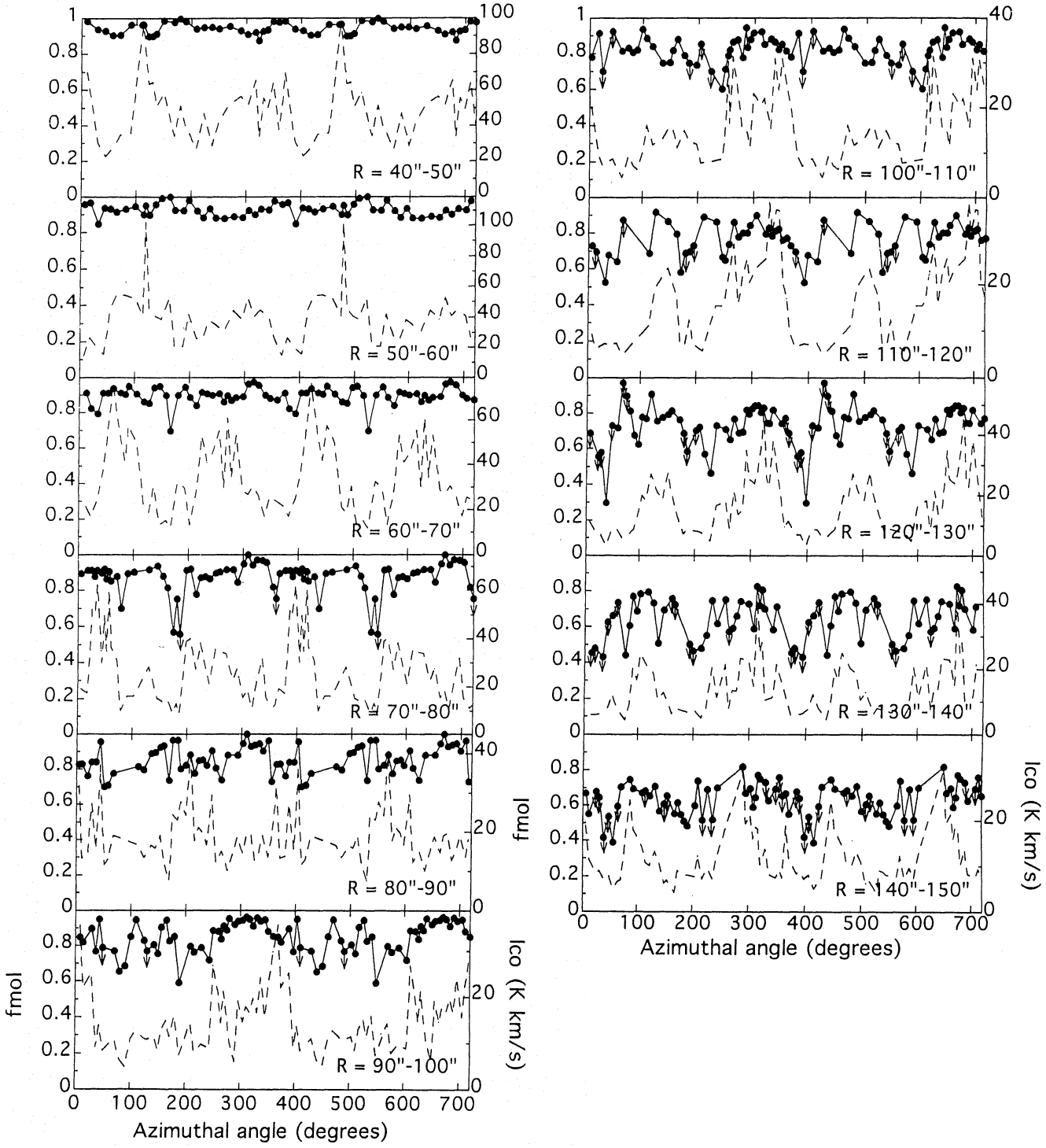

Fig. 7. Azimuthal variations of the molecular mass fraction (solid lines). The definition of the azimuthal angle is the same as in figure 4. The azimuthal variations of the CO integrated intensity are also shown for a comparison (dashed lines).

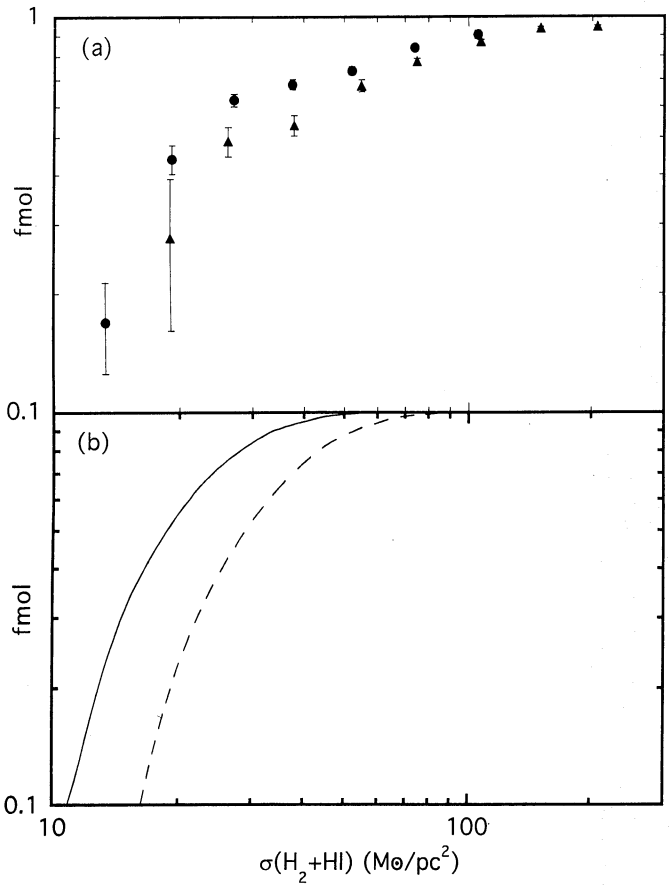

Fig. 8. (a) Dependence of the molecular mass fraction on the total gas surface density, presented separately for the Hα flux density of $F(\mathrm{H}\alpha) < 3.3 \times 10^{-16}$ erg s^{-1} cm^{-2} arcsec^{-2} (circles) and $F(\mathrm{H}\alpha) < 3.3 \times 10^{-16}$ erg s^{-1} cm^{-2} arcsec^{-2} (triangles). (b) Calculated values assuming $F(\mathrm{H}\alpha) = 1.8 \times 10^{-16}$ erg s^{-1} cm^{-2} arcsec^{-2} (solid line) and 7.0×10^{-16} erg s^{-1} cm^{-2} arcsec^{-2} (dashed line), which are the average flux of Hα in each case in (a).

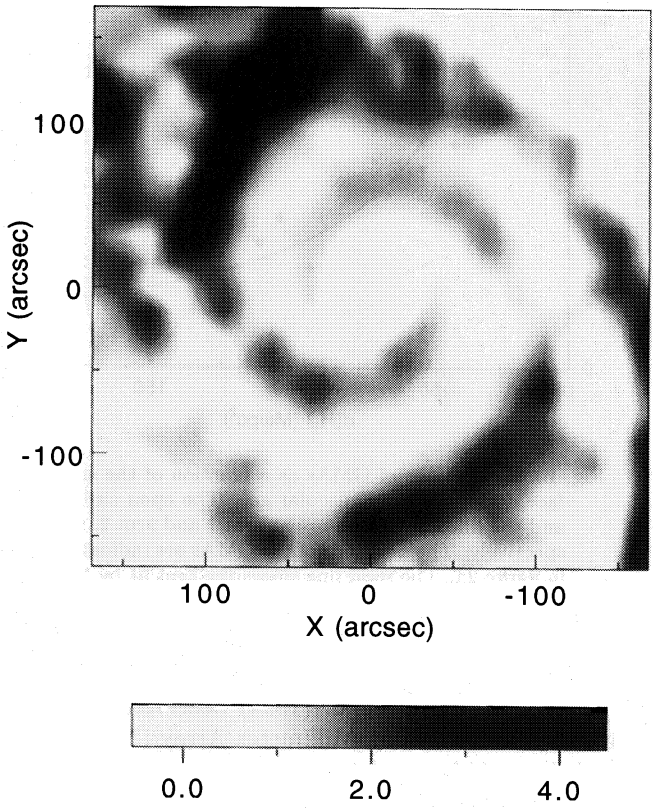

Fig. 9. Gray-scale map of the ratio of the total gas density to the critical density of gravitational instability, $\sigma(\mathrm{H\,I+H_2})/\sigma_c$. The regions where $\sigma(\mathrm{H\,I+H_2})/\sigma_c<1$ are white. The σ_c is calculated from equation (4), adopting the constant rotation velocity of 200 km s^{-1}.

the Galactic conversion factor is larger than our adopted value in M51 by a factor of two to three (subsection 2.1), the criterion for gravitational instability is satisfied even in the interarms, and the velocity dispersion given by the fitting is larger.

To check whether molecular gas has sufficient time to induce a gravitational instability in the crossing spiral arms, we estimate the time scale for the gravitational instability from the Jeans time scale,

$$t_J = \frac{c}{\pi G \sigma}. \quad (6)$$

The time scale for molecular gas in spiral arms is about 1×10^7 yr at $R = 30''$ ($\sigma \approx 130\,M_\odot$ pc^{-2} and $c = 17$ km s^{-1}) and 3×10^7 yr at $R = 150''$ ($\sigma \approx 30\,M_\odot$ pc^{-2} and $c = 11$ km s^{-1}). On the other hand, the molecular arm-crossing time is given by $\tau_{\mathrm{arm}} = d_{\mathrm{arm}}/V_\perp$, where d_{arm} is the arm width and $V_\perp$ the velocity component perpendicular to the arm in the frame corotating with the spiral pattern. The value of d_{arm} has been evaluated from our observations to be about 1 kpc, which is nearly constant through the disk (Paper I). The value of $V_\perp$ is 20 km s^{-1} at $R = 3$ kpc $\approx 65''$ for the adopted pattern speed of $\Omega_p = 14\,\mathrm{km\,s^{-1}kpc^{-1}}$, where the corotation radius is assumed to be at the end of the optical feature ($R \approx 300''$) in M51. Then, for example, $\tau_{\mathrm{arm}} \sim 4.8 \times 10^7$ yr at $R = 3$ kpc. Therefore, the time scale for a gravitational instability is comparable to the arm-crossing time of molecular clouds. However, since the time scale is a lower limit in the case of free-fall, it is not clear whether the arm-crossing time is actually sufficient for the collapse of the gas or not.

4.2. *Random Collisional Agglomeration*

We next examine the possibility of a random collisional agglomeration of smaller clouds into GMAs

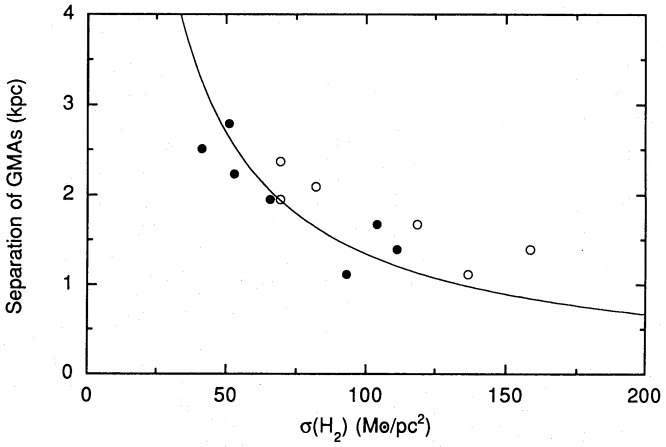

Fig. 10. Separations of GMAs as a function of the surface density of the molecular gas. The open circles and the filled circles represent arm 1 and arm 2, respectively. The positions of the GMAs are indicated in figure 2a. The solid line shows the best fit by the equation (5), giving $c = 12$ km s^{-1}.

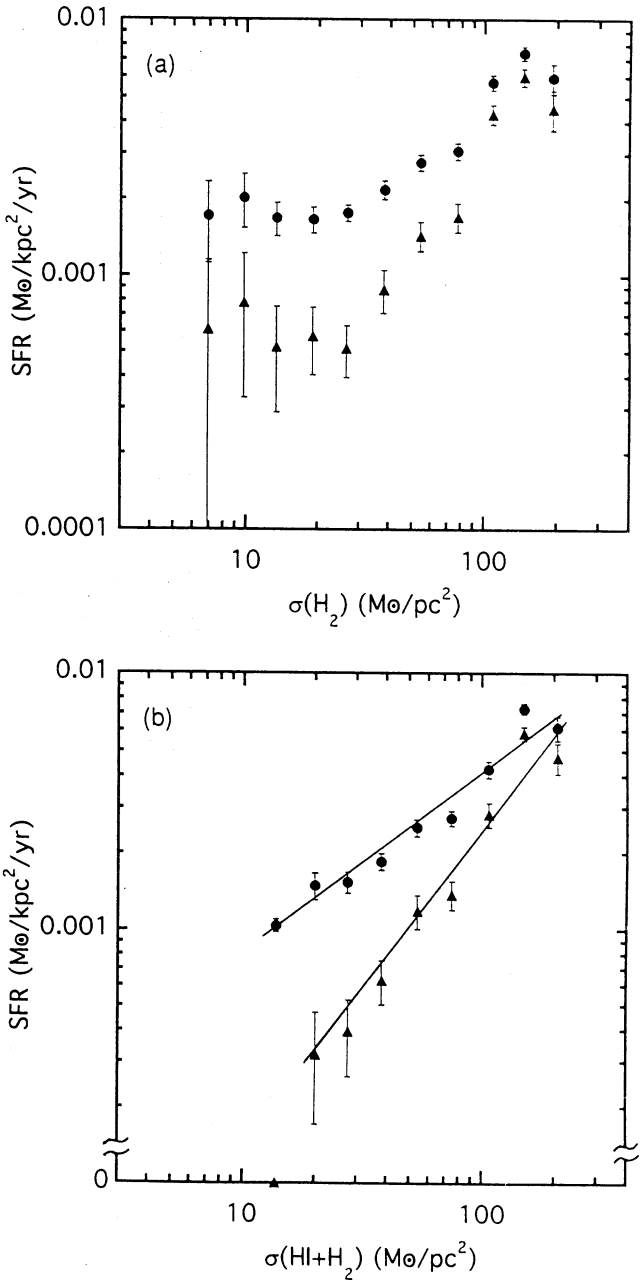

Fig. 11. Dependence of star formation rate on the surface density of the molecular gas (a) and on the surface density of the total gas (b). The circles and the triangles represent the cases with and without the diffuse Hα component, respectively. The solid lines in (b) are the best fit lines with a power law, SFR $\propto$ (H I+H$_2$)^n, and $n = 0.7 \pm 0.1$ for the circles and 1.2 ± 0.5 for the triangles.

(10^7–$10^8\ M_\odot$). Tosaki et al. (1994) observed GMAs in M51 with the Nobeyama Millimeter Array (NMA), and showed that GMAs consist of smaller clouds with a mass of 10^6–$10^7\ M_\odot$, which they called molecular superclouds (MSCs). Moreover, they resolved the MSCs into giant molecular clouds (GMCs) whose mass (10^5–$10^6\ M_\odot$) is comparable to the largest GMCs in our Galaxy. Assuming that the GMAs consist of GMCs, and that most of molecular gas is in the form of GMCs in M51, the same as in our Galaxy, we can estimate the time scale of cloud-cloud collisions in the arms. Since we can not determine the physical parameters of the GMCs in M51, itself, we adopt the average physical parameters of GMCs in our Galaxy: excitation temperature, $T_{\rm ex} = 10$ K; optical depth of CO, $\tau({\rm CO}) \gg 1$; diameter, $D = 40$ pc; velocity dispersion of a cloud, $\Delta V_{\rm c} = 3.8$ km s^{-1} (e.g., Scoville, Sanders 1987); and cloud-cloud velocity dispersion, $c = 12$ km s^{-1}. We can assume two-dimensional motion of the GMCs in the galactic plane, because the diameter of the GMCs is not far from the scale height of the molecular gas (e.g., FWHM $\approx$ 120 pc in the Galaxy; Sanders et al. 1984). Thus, the time scale for cloud-cloud collisions is given by

$$\tau_{\rm coll} \approx \frac{1}{N_{\rm c} s c}, \tag{7}$$

where $N_{\rm c}$ is the surface number density of the GMCs and $s \approx D$ is the collisional cross section. $N_{\rm c}$ pc^{-2} is given by

$$N_{\rm c} = \frac{4f}{\pi D^2}, \tag{8}$$

where f is the filling factor of the GMCs in the telescope beam,

$$f = \frac{T_{\rm mb}\Delta V}{[J(T_{\rm ex}) - J(T_{\rm bg})](1 - e^{-\tau})\Delta V_{\rm c}}, \tag{9}$$

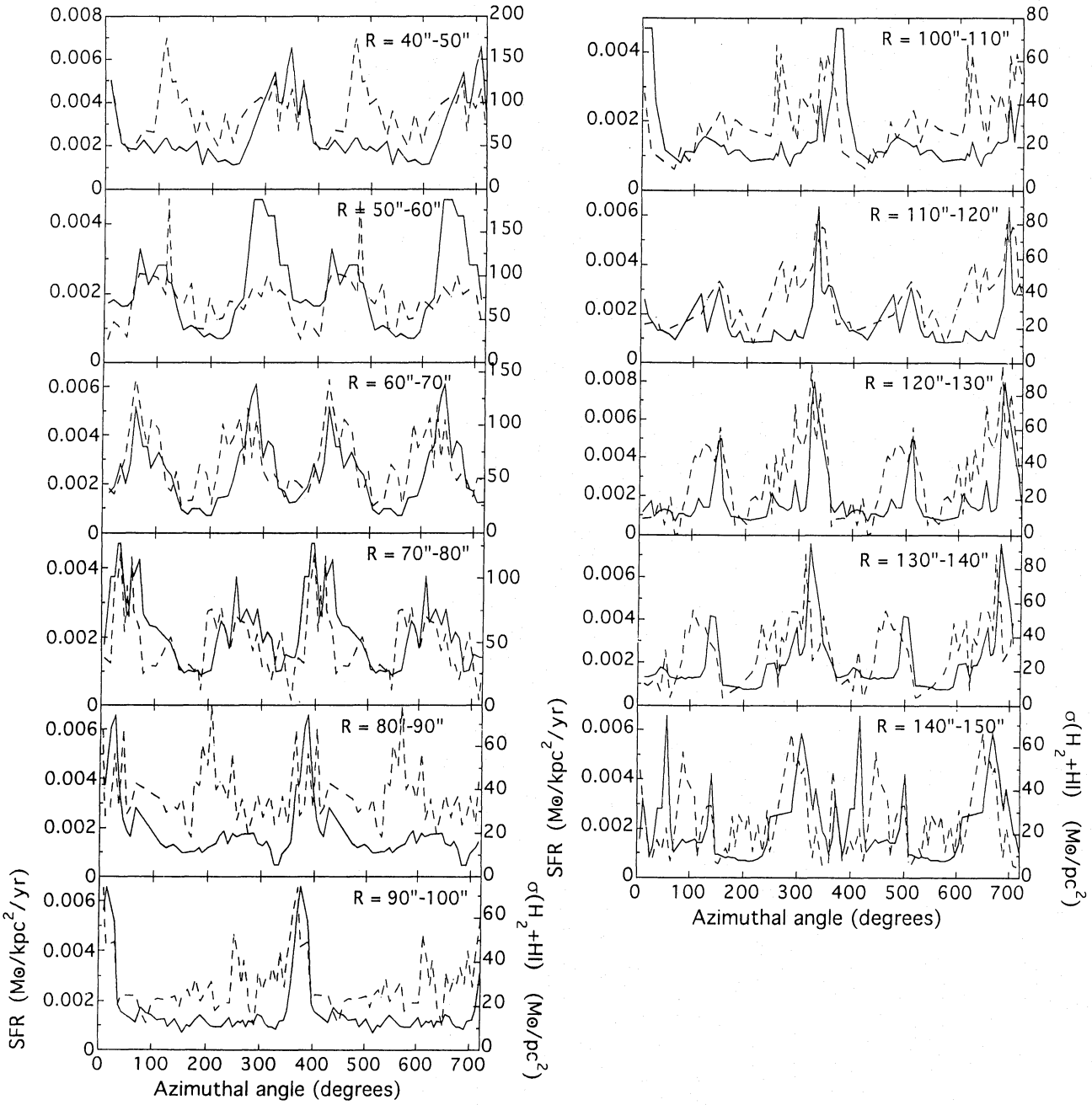

Fig. 12. Azimuthal variations of the star formation rate calculated from the Hα flux density (solid lines) and of the surface density of the total gas σ(H I+H_2) (dashed lines). The definition of the azimuthal angle is the same as figure 4.

where T_{mb} is the main beam brightness temperature (= T_A^*/η_{mb}), T_{bg} (= 2.7 K) the temperature of the cosmic background radiation, ΔV velocity dispersion in a beam and

$$J(T) = \frac{h\nu/k}{\exp(h\nu/kT) - 1}. \quad (10)$$

In most of the arm peaks, T_{mb} is about 1 K; thus, $f = 0.47$ and the number density N_c is 377 kpc^{-2} for $\Delta V = c = 12$ km s^{-1}. Substituting N_c into equation (7), we obtain $\tau_{coll} \sim 5.4 \times 10^6$ yr, which is one order of magnitude shorter than τ_{arm} (4.8×10^7 yr). Moreover, when massive clouds already subsisting in the interarms or massive clouds have grown in the arms, the gravita-

tional influence of the massive clouds enhances the rate of cloud coagulation (Kwan, Valdes 1983). Thus, cloud coagulation could be at work for GMA formation from smaller clouds, like MSCs, perhaps together along with a gravitational instability. The same procedure shows that random collisional agglomeration can form GMCs of $M_{\rm GMC} \sim 10^5\,M_\odot$ from middle clouds of $\sim 10^4\,M_\odot$, but not from very small clouds of $M_{\rm SMC} \sim 10^3\,M_\odot$ directly during the arm-crossing time.

5. Formation of Massive Stars

Here, we examine the mechanisms of massive star formation from interstellar gas. First, we check which is correlated with the star-formation rate (SFR), the molecular gas density $\sigma(\rm H_2)$ or the total gas density $\sigma(\rm H\,I{+}H_2)$. SFR for $M \geq 10\,M_\odot$ is derived by the following equation (Kennicutt 1983):

$$\mathrm{SFR}(\geq 10\,M_\odot) = \frac{L(\mathrm{H}\alpha)}{7.02 \times 10^{41}\ \mathrm{erg\ s^{-1}}}\ M_\odot\ \mathrm{yr^{-1}}, \quad (11)$$

where L (Hα) is the luminosity of Hα emission in erg s^{-1}. We used the Hα flux of Tully (1974a) after convolution to make the resolution the same as our CO data. Figure 11 shows the resultant relation between SFR and $\sigma(\rm H_2)$ or $\sigma(\rm H\,I{+}H_2)$. The correlation between $\sigma(\rm H_2)$ and SFR is worse in the region of low $\sigma(\rm H_2)$ ($< 20\,M_\odot$). On the other hand, the correlation between $\sigma(\rm H\,I{+}H_2)$ and SFR can be easily fitted by a straight line of SFR $(M_\odot\ \mathrm{kpc^{-2}yr^{-1}}) = (1.7 \pm 0.6) \times 10^{-4}\ \sigma(\rm H\,I{+}H_2)^{0.7\pm0.1}$. The data of Tully (1974a) seems to have uniform background radiation of Hα (figure 2c). Rand (1992) calculated the contribution of the diffuse ionized component to the Hα total luminosity to be 50% (1×10^{41} erg s^{-1}). In fact, in the data of Tully (1974a), the Hα flux in the interarms is almost constant at around 1.3×10^{-16} erg s^{-1}cm^{-2}arcsec^{-2}, which is independent of the total gas density (see below). Since the faint and uniform component may not be directly related to massive stars, they may be caused by general radiation in the interstellar field; we can thus remove the uniform component (1.3×10^{-16} erg s^{-1}cm^{-2}arcsec^{-2}) from the total Hα flux. The triangles in figure 11 show the resultant relation between SFR and $\sigma(\rm H_2)$ or $\sigma(\rm H\,I{+}H_2)$. Again, SFR is more correlated with $\sigma(\rm H\,I{+}H_2)$ than $\sigma(\rm H_2)$. The best fit, except for the point SFR = 0, gives SFR $(M_\odot\ \mathrm{kpc^{-2}yr^{-1}}) = (8.7 \pm 2.2) \times 10^{-5}\ \sigma(\rm H\,I{+}H_2)^{1.2\pm0.5}$. Here, we do not correct the extinction. If we use the empirical relation in the Galaxy, A_V mag $= 5.4 \times 10^{-22}\ N(\rm H\,I{+}H_2)$ cm^{-2} (Bohlin et al. 1978), SFR must be multiplied by 1.37 at a surface density of $10\,M_\odot$ pc^{-2} and 533 at $200\,M_\odot$ pc^{-2}. As a result, the above power becomes larger. However, the uncertainty of the correction is large, because we assume that the gas distributes uniformly in a 16″ beam, and covers the H II regions entirely.

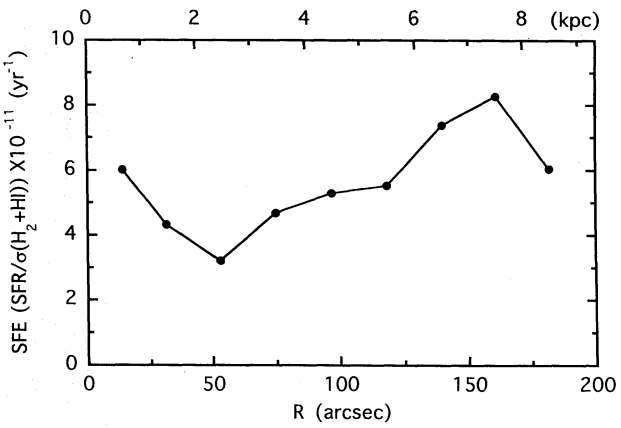

Fig. 13. Radial variations of the star-formation efficiency, SFR/$\sigma(\rm H\,I{+}H_2)$ yr^{-1}.

If the gas has clumpy structures, and does not cover the H II regions, the correction factor is overestimated.

Figure 12 shows the azimuthal variations in the Hα flux and the total gas density. Generally, the Hα flux is correlated with the total gas density in the azimuthal variations. In more detail, however, there are some noticeable properties between the two gases: (1) The Hα flux in the interarm is almost constant, independent of the total gas density (as mentioned above). This implies that the diffuse ionized component is dominant in the interarms. (2) The arm-to-interarm ratio of Hα is almost the same as that of the total gas density. If the diffuse ionized component is removed and the larger extinction in the arms is considered, however, the arm-to-interarm ratio of Hα is larger than that of the total gas density, as shown by Rand (1992). (3) The Hα arms are narrower than the arms of the total gas, and are located in the downstream side in the arms of the total gas (also see subsection 2.3), especially in the outer regions (R = 90″–140″), where the spiral arms are easily resolved. This feature indicates that SFE suddenly increases in the middle of the arms of the total gas. This is evidence that a density wave triggers star formation, as pointed out for M51 by Rand (1993), by increasing the gas density or the number density of molecular clouds in the spiral arms. There are two candidates of trigger processes. The first is a large-scale gravitational instability. The surface density of the total gas in the arms exceeds the critical density for gravitational instability ($\sigma_{\rm c}$; figure 9). Since the instability seems to induce the formation of massive stars (figure 11 and Kennicutt 1989), SFE is enhanced in the arms. The second possibility is cloud-cloud collisions. GMCs collide with each other when they are crossing a spiral arm (section 5). Probably, actual star formation in the spiral arms is enhanced by a combination of these possibilities.

Table 4. Line parameters of ^{12}CO, ^{13}CO, and HCN.

Position $\Delta\alpha$	Position $\Delta\delta$	A/I*	I (^{12}CO) (K km s^{-1})	I (^{13}CO)† (K km s^{-1})	I (HCN)† (K km s^{-1})	^{12}CO/^{13}CO	^{12}CO/HCN	^{13}CO/HCN
−51.″3	−54.″7	I	15.2 ± 3.5	< 0.90	< 0.59	> 16.9	> 25.8	...
−22.6	41.7	I	42.7 ± 2.0	1.71 ± 0.20	< 0.22	25.0 ± 3.1	> 194	> 7.8
28.7	−33.0	I	27.5 ± 2.7	1.11 ± 0.21	< 0.53	24.8 ± 5.3	> 51.9	> 2.1
53.9	40.0	I	31.9 ± 2.9	< 0.71	< 0.92	> 44.9	> 34.7	...
−7.0	−46.9	A	95.1 ± 2.9	7.25 ± 0.51	1.05 ± 0.48	13.1 ± 1.0	90.6 ± 41.5	6.9 ± 3.2
7.0	46.9	A	44.4 ± 1.8	3.82 ± 0.54	0.84 ± 0.10	11.6 ± 1.7	52.9 ± 6.7	4.5 ± 0.8
40.0	−53.9	A	67.7 ± 1.7	4.64 ± 0.51	1.23 ± 0.21	14.6 ± 1.6	55.0 ± 9.5	3.8 ± 0.8
66.9	−33.9	A	34.9 ± 1.7	2.52 ± 0.31	...	13.8 ± 1.8	...	...

* A and I indicate arm and interarm, respectively.
† Upper limits are 2σ. In that case, the velocity widths are assumed to be the same as ^{12}CO.

Figure 13 shows the radial variation of SFE (SFR/$\sigma_{\rm total}$). The mean value at $R < 8.5$ kpc is SFE = 5×10^{-11} yr^{-1}. However, SFE is not constant throughout the disk, but shows a peak at around $R \approx 7$ kpc. This is caused by an enhanced star-formation rate in the NE part of the disk at $R \approx 7$ kpc. This is apparent from the distribution of H II regions shown in figure 2c. Lord and Young (1989) suggested that the local enhancement of star formation in the region is due to an encounter with the companion galaxy NGC 5195. The enhancement in the gas density (figure 1) and the velocity dispersion in the NE part due to the encounter seems to have induced star-burst activity.

6. ^{13}CO and HCN in M51

We investigated the physical properties of molecular gas in the arms and the interarms by observing the ^{13}CO line, which is optically thin, and the HCN line, which traces dense molecular gas ($> 10^5$ cm^{-3}).

6.1. ^{13}CO and HCN Observations

Observations of the ^{13}CO ($J=1$–0) and HCN ($J=1$–0) emissions were made in 1992 April and May with the Nobeyama 45-m telescope. The half-power beam widths of the telescope were 20″ at the HCN frequency (88.632 GHz) and 17″ at the ^{13}CO frequency (110.201 GHz). The aperture and main-beam efficiencies were $\eta_{\rm a} = 0.37$ (110 GHz) and 0.43 (86 GHz), and $\eta_{\rm mb} = 0.52$ (110 GHz) and 0.54 (86 GHz), respectively (table 2). These two lines were observed simultaneously using two SIS receivers. The beam squint between the two receivers was $\leq 1''$. The system noise temperatures (SSB) at 88.6 GHz and 110.2 GHz, including the atmospheric effect and the antenna ohmic loss, were 300–500 K and 500–700 K, respectively. The observations were made in the position-switching mode. The telescope pointing was checked and calibrated every hour by observing a SiO maser star, R Cvn. The absolute pointing accuracy was better than ±5″ (peak value) throughout the observations. We observed 4 points in the arms and 4 points in the interarms for ^{13}CO and 3 points in the arms and 4 points in the interarms for HCN. The observed positions are indicated in figure 14. The measured spectra are shown in figure 15 and the line parameters are listed in table 4.

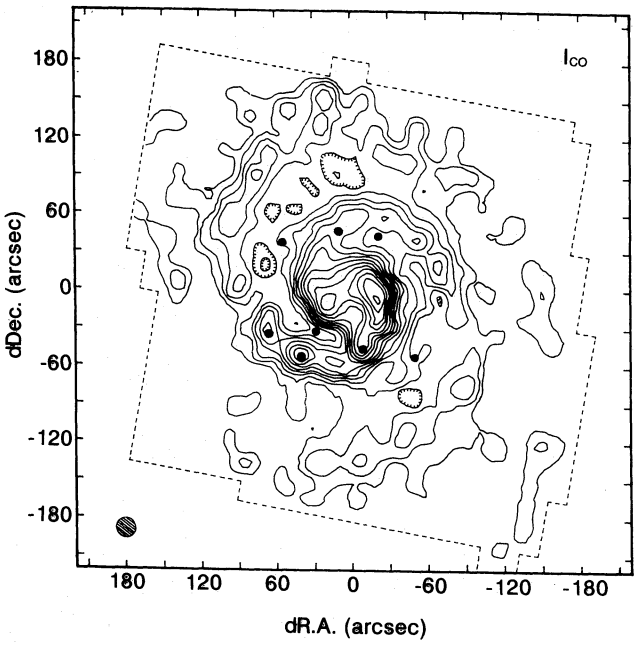

Fig. 14. Positions of the observed points of ^{13}CO and HCN (dots) on the contour map of ^{12}CO.

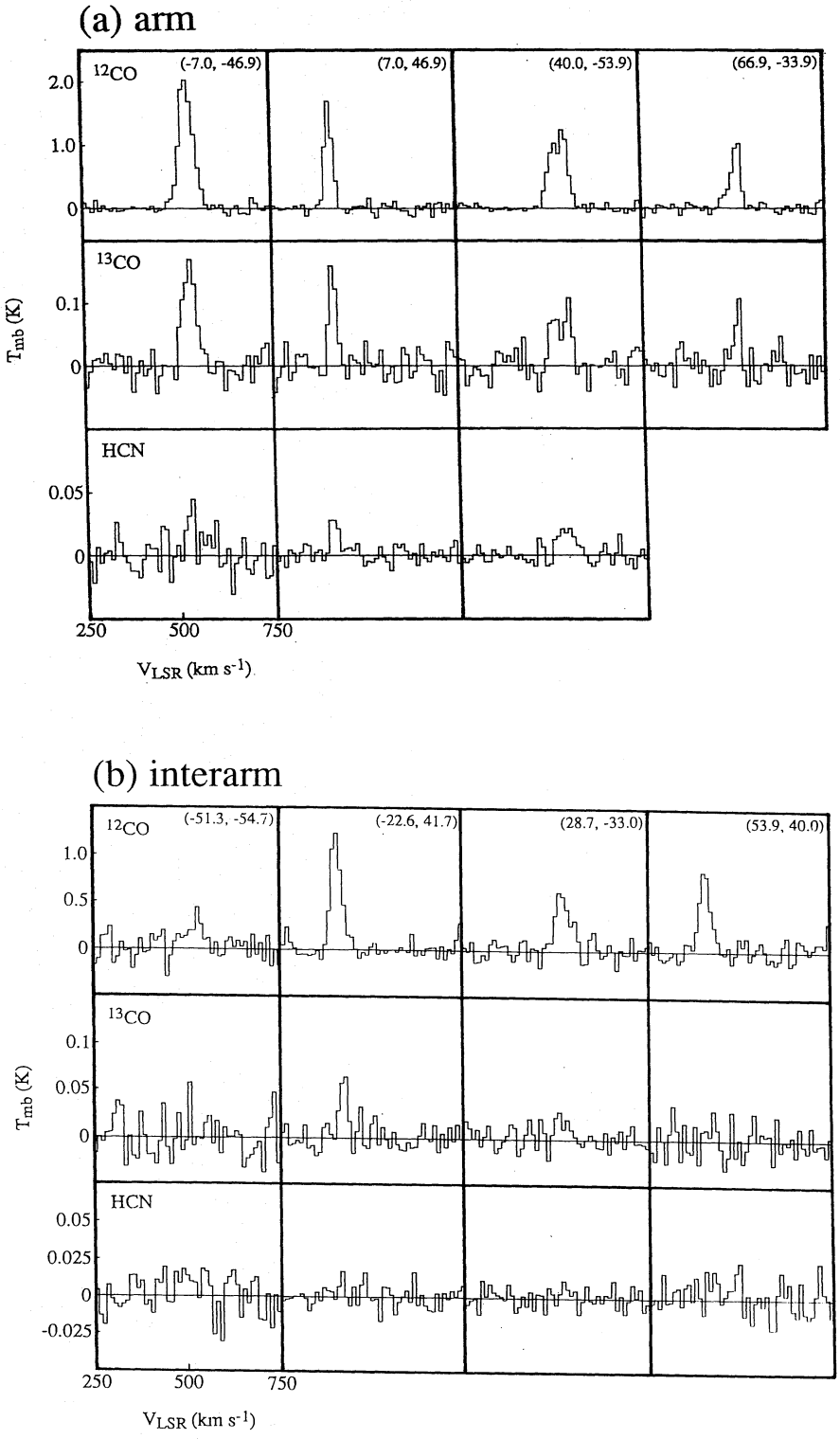

Fig. 15. Spectra of ^{12}CO, ^{13}CO, and HCN emissions in the arms (a) and in the interarms (b). Coordinates of the observed positions ($\Delta\alpha$, $\Delta\delta$) are indicated at the top right in the boxes of ^{12}CO spectra.

6.2. Dense Molecular Gas in M51

We detected ^{13}CO at all points in the arms and two points in the interarms. The line profiles are almost the same as those of ^{12}CO. The temperature ratio of ^{12}CO/^{13}CO in the arms is about 13, which is consistent with other results (Young, Sanders 1986; Encrenaz et al. 1979). If we assume that the excitation temperature (T_{ex}) of ^{13}CO is the same as that of ^{12}CO, the ratio gives the optical depth of $\tau(^{12}\mathrm{CO}) \approx 5$ and $\tau(^{13}\mathrm{CO}) \approx 0.08$ for an abundance ratio of ^{12}CO/^{13}CO = 60. On the other hand, the ^{12}CO/^{13}CO ratio in the interarms (≈ 25) is about twice of that in the arms, indicating that $\tau(^{12}\mathrm{CO}) \approx 2$ and $\tau(^{13}\mathrm{CO}) \approx 0.03$. This means that ^{12}CO in the interarms is less optically thick than in the arms. This may also mean that the diffuse component of molecular gas is more dominant in the interarms, as suggested by García-Burillo et al. (1993a).

We detected HCN at all points in the arms, but not at any points in the interarms. The temperature ratios of ^{12}CO/ HCN in the arms are 40–90, which are much larger than 12 in the central region of M51 (Nguyen et al. 1992). The noise levels in the interarms are not small enough to be compared with the ratio in the arms, except for one point at (−22.6, 41.7). The lower limit at the point is 194, which is larger than that in the arms. Since HCN is considered to trace dense molecular gas ($> 10^5$ cm^{-3}), this means that the fraction of the dense molecular gas to the total molecular gas in the arms is higher than that in the interarms. This is consistent with the results derived from the ^{12}CO/^{13}CO ratio. Here, we observed only 3–4 points in the spiral arms and the interarms, each. Further observations of both regions are required in order to compare the physical state of molecular gas in the arms and interarms.

7. Summary

The concluding remarks are summarized as follows:

(1) The arm-to-interarm ratio of the CO integrated intensity is 1.5–7 at 2 kpc $< R <$ 7 kpc.

(2) The mass fraction of the molecular gas (H_2) to the total gas (H I+H_2) increases along with the total gas density, and decreases along with the intensity of the radiation field. Thus, the molecular gas dominates in the inner disk and the fraction decreases outward. In the outer region, $R > 100''$, where the arm-to-interarm ratio of the gas density is large, the fraction is also larger in the arms (0.7–0.9) than in the interarms (< 0.7), while the fraction is almost constant in the inner region with the small arm-to-interarm ratio of the gas density.

(3) The surface density of the total gas exceeds the critical density of the gravitational instability (σ_c) in the spiral arms, but not in most of the interarms. The spatial separations of GMAs agree with the wavelength of the fastest growing mode of the gravitational instability. These results support the gravitational instability as being the formation mechanism of GMAs.

(4) Since the time scale of cloud-cloud collisions in the arms are one order of magnitude shorter than the arm-crossing time of molecular clouds, cloud-cloud collisions occur in the arms frequently when the clouds cross an arm. Thus, cloud coagulation may also work for GMA formation together with a gravitational instability.

(5) The star-formation rate (SFR) correlates with the surface density of the total gas better than that of molecular gas alone. SFR depends on the total gas density with a power of 1.2 without any correction for extinction.

(6) The star-formation efficiency (SFE = SFR/gas density) in the arms is higher than in the interarms. The results of (3) and (5) suggest that the enhanced SFE in the arms could be caused by a large-scale gravitational instability in the arms: since the surface density of the total gas exceeds σ_c in the arms and does not exceed in the interarms, SFE in the arms is enhanced, if massive star formation is induced by a large-scale gravitational instability. Since the time scale of cloud-cloud collisions in the arms are much shorter than the arm crossing time of a molecular cloud, cloud-cloud collisions may also contribute to star formation in the arms.

(7) The ^{12}CO/^{13}CO and ^{12}CO/HCN ratios in the arms and the interarms suggest that the molecular gas is optically thicker in the arms than in the interarms, due to the denser gas density in the arms. Since the observed points were only 3–4 in the spiral arms and interarms each, further studies are necessary to confirm the results.

We thank A.H. Rots for providing H I data with the same resolution as our CO data. We also thank the staff members of the Nobeyama Radio Observatory for encouragement to carry out this project.

References

Adler D.S., Lo K.Y., Wright M.C.H., Rydbeck G., Plante R.L., Allen R.J. 1992, ApJ 392, 497

Bloemen J.B.G.M., Caraveo P.A., Hermsen W., Lebrun F., Maddalena R.J., Strong A.W., Thaddeus P. 1984, A&A 139, 37

Bohlin R.C., Savage B.D., Drake J.F. 1978, ApJ 224, 132

Combes F., Gerin M. 1985, A&A 150, 327

de Vaucouleurs G., de Vaucouleurs A., Corwin H.G.Jr, Buta R.J., Paturel G., Fougué P. 1991, Third Reference Catalogue of Bright Glaxies (Springer-Verlag, New York)

Elmegreen B.G. 1990a, ApJ 357, 125

Elmegreen B.G. 1990b, in The Evolution of the Interstellar Medium, ed L. Blitz, PASPC 12, 247

Elmegreen B.G. 1991, ApJ 378, 139

Elmegreen B.G. 1993a, in Star Formation, Galaxies and the Interstellar Medium, ed J. Franco, F. Ferrini, G. Tenorio-Tagle (Cambridge University Press, Cambridge) p337

Elmegreen B.G. 1993b, ApJ 411, 170
Elmegreen B.G. 1994, in Physics of the Gaseous and Stellar Disks of the Galaxy, ed I. King, PASPC 66, 61
Elmegreen B.G., Elmegreen D.M. 1983, MNRAS 203, 31
Elmegreen D.M., Elmegreen B.G., Lang C., Stephens C. 1994, ApJ 425, 57
Encrenaz P.J., Stark A.A., Combes F., Wilson R.W. 1979, A&A 78, L1
Federman S.R., Glassgold A.E., Kwan J. 1979, ApJ 227, 466
Ford H.C., Crane P.C., Jacoby G.H., Lawrie D.G., van der Hulst J.M. 1985, ApJ 293, 132
García-Burillo S., Combes F., Gerin M. 1993b, A&A 274, 148
García-Burillo S., Guélin M., Cernicharo J. 1993a, A&A 274, 123
Howard S., Byrd G.G. 1990, AJ 99, 1798
Kennicutt R.C. 1983, ApJ 272, 54
Kennicutt R.C. 1989, ApJ 344, 685
Klein U., Wielebinski R., Beck R. 1984, A&A 135, 213
Kwan J. 1979, ApJ 229, 567
Kwan J., Valdes F. 1983, ApJ 271, 604
Lord S.D., Young J.S. 1990, ApJ 356, 135
Mathewson D.S., van der Kruit P.C., Brouw W.N. 1972, A&A 17, 468
Mouschovias T.C., Shu F.H., Woodward P.R. 1974, A&A 33, 73
Nakai N., Kuno N. 1995, PASJ 47, 761
Nakai N., Kuno N., Handa T., Sofue Y. 1994, PASJ 46, 527 (Paper I)
Nguyen Q-Rieu, Jackson J.M., Henkel C., Bach T., Mauersberger R. 1992, ApJ 399, 521
Parker E.N. 1966, ApJ 145, 811
Rand R.J. 1992, AJ 103, 815
Rand R.J. 1993, ApJ 410, 68
Rand R.J., Kulkarni S.R. 1990, ApJL 349, L43
Reynolds R.J. 1984, ApJ 282, 191
Rots A.H., Bosma A., van der Hulst J.M., Athanassoula E., Crane P.C. 1990, AJ 100, 387
Rydbeck G., Hjalmarson Å., Rydbeck O.E.H. 1985, A&A 144, 282
Sandage A., Tammann G.A. 1974, ApJ 194, 559
Sandage A., Tammann G.A. 1981, A Revised Shapley-Ames Catalog of Bright Galaxies (Carnegie Institution of Washington, Washington, D.C.)
Sanders D.B., Solomon P.M., Scovile N.Z. 1984, ApJ 276, 182
Scovile N.Z., Sanders D.B. 1987, in Interstellar Processes, ed D.J. Hollenbach, H.A. Thronson (D. Reidel Publishing Company, Dordrecht) p21
Scoville N.Z., Sanders D.B., Clemens D.P. 1986, ApJL 310, L77
Segalovitz A. 1977, A&A 54, 703
Shaver P.A., McGee R.X., Newton L.M., Danks A.C., Pottasch S.R. 1983, MNRAS 204, 53
Solomon P.M., Rivolo A.R., Barrett J., Yahil A. 1987, ApJ 319, 730
Tilanus R.P.J., Allen R.J. 1989, ApJL 339, L57
Tilanus R.P.J., Allen R.J. 1991, A&A 244, 8
Toomre A. 1964, ApJ 139, 1217
Tosaki T., Taniguchi Y., Kawabe R. 1994, ApJ submitted
Tully R.B. 1974a, ApJS 27, 415
Tully R.B. 1974b, ApJS 27, 437
Tully R.B. 1974c, ApJS 27, 449
van der Hulst J.M., Kennicutt R.C., Crane P.C., Rots A.H. 1988, A&A 195, 38
Vogel S.N., Kulkarni S.R., Scoville N.Z. 1988, Nature 334, 402
Woodward P.R. 1976, ApJ 207, 484
Young J.S., Sanders D.B. 1986, ApJ 302, 680
Zaritsky D., Kennicutt R.C., Huchra J.P. 1994, ApJ 420, 87